LETTER

https://doi.org/10.1038/s41586-019-1248-6

Cryo–EM structures of herpes simplex virus type 1 portal vertex and packaged genome

Yun-Tao Liu[1,2,3,6], Jonathan Jih[3,6], Xinghong Dai[3,4,5], Guo-Qiang Bi[1,2] & Z. Hong Zhou[3,4,5]*

Herpesviruses are enveloped viruses that are prevalent in the human population and are responsible for diverse pathologies, including cold sores, birth defects and cancers. They are characterized by a highly pressurized pseudo-icosahedral capsid—with triangulation number (*T*) equal to 16—encapsidating a tightly packed double-stranded DNA (dsDNA) genome[1–3]. A key process in the herpesvirus life cycle involves the recruitment of an ATP-driven terminase to a unique portal vertex to recognize, package and cleave concatemeric dsDNA, ultimately giving rise to a pressurized, genome-containing virion[4,5]. Although this process has been studied in dsDNA phages[6–9]—with which herpesviruses bear some similarities—a lack of high-resolution in situ structures of genome-packaging machinery has prevented the elucidation of how these multi-step reactions, which require close coordination among multiple actors, occur in an integrated environment. To better define the structural basis of genome packaging and organization in herpes simplex virus type 1 (HSV-1), we developed sequential localized classification and symmetry relaxation methods to process cryo-electron microscopy (cryo-EM) images of HSV-1 virions, which enabled us to decouple and reconstruct hetero-symmetric and asymmetric elements within the pseudo-icosahedral capsid. Here we present in situ structures of the unique portal vertex, genomic termini and ordered dsDNA coils in the capsid spooled around a disordered dsDNA core. We identify tentacle-like helices and a globular complex capping the portal vertex that is not observed in phages, indicative of herpesvirus-specific adaptations in the DNA-packaging process. Finally, our atomic models of portal vertex elements reveal how the fivefold-related capsid accommodates symmetry mismatch imparted by the dodecameric portal—a longstanding mystery in icosahedral viruses—and inform possible DNA-sequence recognition and headful-sensing pathways involved in genome packaging. This work showcases how to resolve symmetry-mismatched elements in a large eukaryotic virus and provides insights into the mechanisms of herpesvirus genome packaging.

Applying our method of symmetry relaxation, we first distinguished between the unique portal vertex and the eleven penton vertices for each capsid, obtaining a 4.3 Å resolution structure of the portal vertex region with fivefold (C5) symmetry (Extended Data Table 1, Extended Data Figs. 1, 2). Subsequent rounds of sequential localized classification and sub-particle reconstruction yielded four other reconstructions: a 12-fold-symmetric (C12) reconstruction of the dodecameric portal (Extended Data Fig. 2a, e) and asymmetric (C1) reconstructions of the portal vertex region (Extended Data Fig. 2a, d), genome-containing virion (Extended Data Fig. 2a, f) and genome terminus in the DNA translocation channel (Extended Data Fig. 2b, g, Extended Data Table 1). Segmenting and aligning these reconstructions enables the simultaneous visualization of all elements in the capsid-associated tegument complex (CATC)-decorated, genome-containing capsid (Fig. 1a, Supplementary Video 1).

Our C1 virion reconstruction reveals ordered, concentric dsDNA shells spooled in a left-handed manner around a disordered, ellipsoidal core of dsDNA (Fig. 1b). Up to ten concentrically equidistant layers are distinguishable, which we denote alphabetically from the outside in Fig. 1c. As expected given the extreme space constraints within the capsid, inter- and intra-layer dsDNA strands exhibit a space-efficient honeycomb topology, consistent with indications of near-crystalline genomic packing in many dsDNA viruses[10,11]. Two other genomic structures are visible at the portal vertex. An asymmetric serpent-like density exhibiting major grooves and two distinctive right-handed

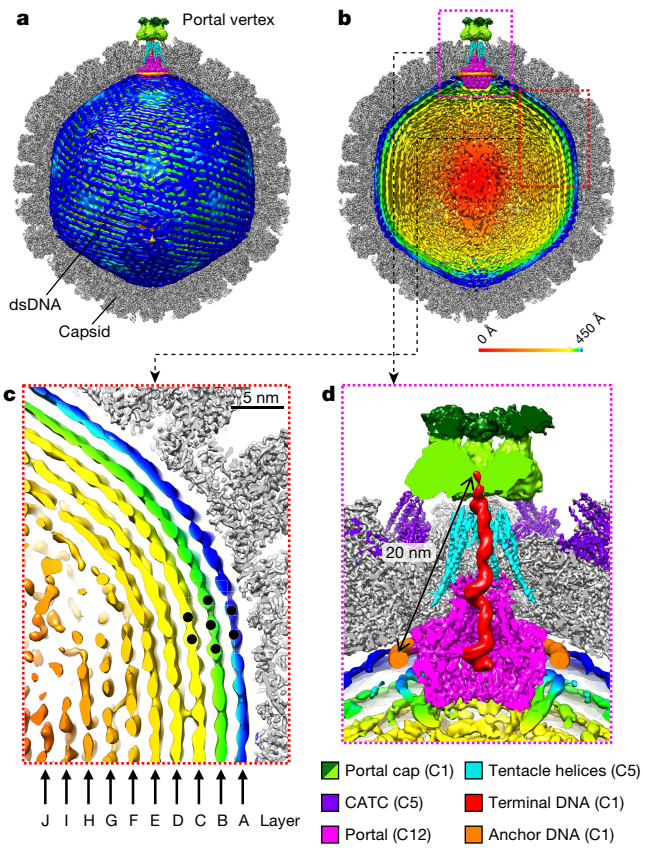

Fig. 1 | Structures of the portal vertex and dsDNA genome. a, Composite structure showing capsid (*z*-clipped), left-handed-spooled dsDNA genome and portal vertex elements. **b**, Same view as **a**, but with dsDNA (radially coloured) *z*-clipped, revealing concentric shells of dsDNA density around a disordered core. **c**, Red inset from **b** reveals ten layers of near-crystalline, honeycomb-packed dsDNA. **d**, Magenta inset from **b** illustrates portal vertex structures. See Supplementary Video 1.

[1]Center for Integrative Imaging, Hefei National Laboratory for Physical Sciences at the Microscale, University of Science and Technology of China, Hefei, China. [2]School of Life Sciences, University of Science and Technology of China, Hefei, China. [3]California NanoSystems Institute (CNSI), University of California, Los Angeles, Los Angeles, CA, USA. [4]Department of Microbiology, Immunology and Molecular Genetics, University of California, Los Angeles, Los Angeles, CA, USA. [5]Department of Molecular and Medical Pharmacology, University of California, Los Angeles, Los Angeles, CA, USA. [6]These authors contributed equally: Yun-Tao Liu, Jonathan Jih. *e-mail: hong.zhou@ucla.edu

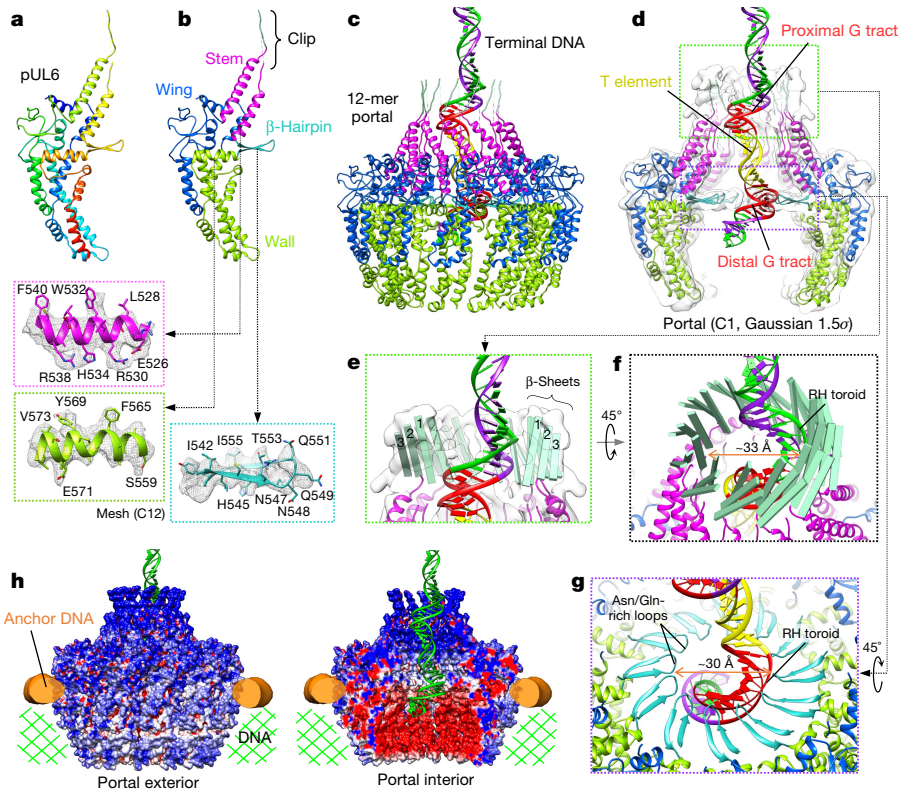

Fig. 2 | pUL6 portal structure and interactions with dsDNA. **a**, **b**, pUL6 atomic models coloured in rainbow (red (N terminus) to blue (C terminus)) (**a**) and by domain (**b**). Insets show ribbon-and-stick models in mesh density (C12 portal reconstruction). **c**, Terminal DNA threads through a dodecameric portal comprising twelve pUL6 monomers. **d**, *z*-clipped portal shown with C1 density (portal vertex reconstruction) Gaussian-filtered to 1.5σ to show clip structure. Terminal DNA contains two right-handed toroidal regions, each containing a conserved G tract, flanking a spacer T element. **e**, Green inset from **d** shows three-stranded β-sheets in each pUL6 monomer clip. **f**, Twelve three-stranded β-sheets form a right-handed (RH)-twisted turret in the clip, which interacts with proximal toroidal DNA. **g**, Purple inset from **d** shows twelve β-hairpins forming an apertured disk through which distal toroidal DNA passes. **h**, Electrostatic-surface renderings of the portal in a DNA environment. Blue, positive charge; red, negative charge. See Supplementary Videos 2 and 3.

toroidal regions occupying the portal vertex channel extending from the base of the portal to a portal vertex-capping density (Fig. 1d). On the basis of phage studies indicating that the viral genomic end is positioned in this way to poise the genome for ejection[7,10] and as well as the consensus that the last-packaged end is the first to be ejected[12], we interpret this serpent-like density to be the last-packaged end of the HSV-1 genome and name it 'terminal DNA'. In close proximity to this terminal DNA, a ringed density exhibits faint groove-like patterns and encircles the base of the dodecameric portal (Fig. 1d). Notably, this ringed density is exceptionally strong relative to adjacent concentric genomic density, indicative of a particularly strong and perhaps specific association with the portal. A previous study demonstrated that the genomic ends of T4 phage are consistently localized to maintain a 9-nm separation[13]. As the HSV-1 portal vertex contains approximately 11-nm long 'tentacle helices' for which T4 has no analogues, the approximately 20-nm distance between the last-packaged end of terminal DNA and the portal-anchored ringed density suggest that the ringed density is the first-packaged anchoring segment of genome. We therefore name this density 'anchor DNA'.

Next, we atomically modelled pUL6 using our C12 portal reconstruction (Fig. 2a, Extended Data Table 1). Structurally, each 676-residue pUL6 monomer consists of five domains—wing (residues 33–62 and 150–271), stem (residues 272–300 and 517–540), clip (residues 301–516, although residues 308–516 are unmodelled), β-hairpin (residues 541–558) and wall (residues 63–149 and 559–623)—and unresolved N- and C-terminal stretches of 32 and 53 residues, respectively (Fig. 2b, Extended Data Fig. 3 and Supplementary Video 2). Twelve pUL6 monomers constitute the portal and are arranged such that their loop-rich wing domains form the outer periphery of the complex (Fig. 2c). The remaining stem, clip, β-hairpin and wall domains line the interior of the portal's DNA translocation channel (Fig. 2d).

Within the translocation channel, the aforementioned terminal DNA extends outwards, terminating within the bell-like portal cap (Fig. 1d). Taking this as the site of concatemeric cleavage, we used our C1 reconstruction of terminal DNA to generate a density-fitted three-dimensional model of the final 67-base pair (bp) stretch of HSV-1 genome terminus, comprising the 3′ overhang of the cleavage site, a single base pair of directly repeated elements (DR1) preceding the cleavage site, and the preceding 66-bp stretch of unique sequence (Ub)[14–16] (Fig. 2d, Extended Data Fig. 4, Supplementary Video 3). Within the 66-bp Ub sequence, a stretch consisting of *pac1* T element flanked by two short G tracts (GGGGGG and GGGGGGGG from *pac1* proximal and distal GC elements of Ub, respectively) forms the major conserved motif at the termini of herpesvirus genomes, constituting the minimal sequence necessary for proper concatemeric cleavage[17,18]. Whereas both flanking G tracts are critical to the sequence, the T element tolerates substitutions, but not deletions, suggesting that it may function as a regulatory spacer element[15]. Notably, proximal and distal G tracts in our fitted model map to the two right-handed toroidal densities of terminal DNA, which contact the interior walls of the portal channel, whereas the T element occupies a straight segment of density that exhibits no such contacts (Fig. 2d, Extended Data Fig. 4). Although both the structure and the model reflect a packaged state, our structure and model may be circumstantial evidence of sequence sensitivity of the portal during genome packaging.

On the portal side, contacts with proximal and distal toroids of terminal DNA occur through clip and β-hairpin domains, both of which contain distinctive β-sheet motifs. Density of the clip is visible at lower thresholds in our C1 reconstructions, but is disordered in our

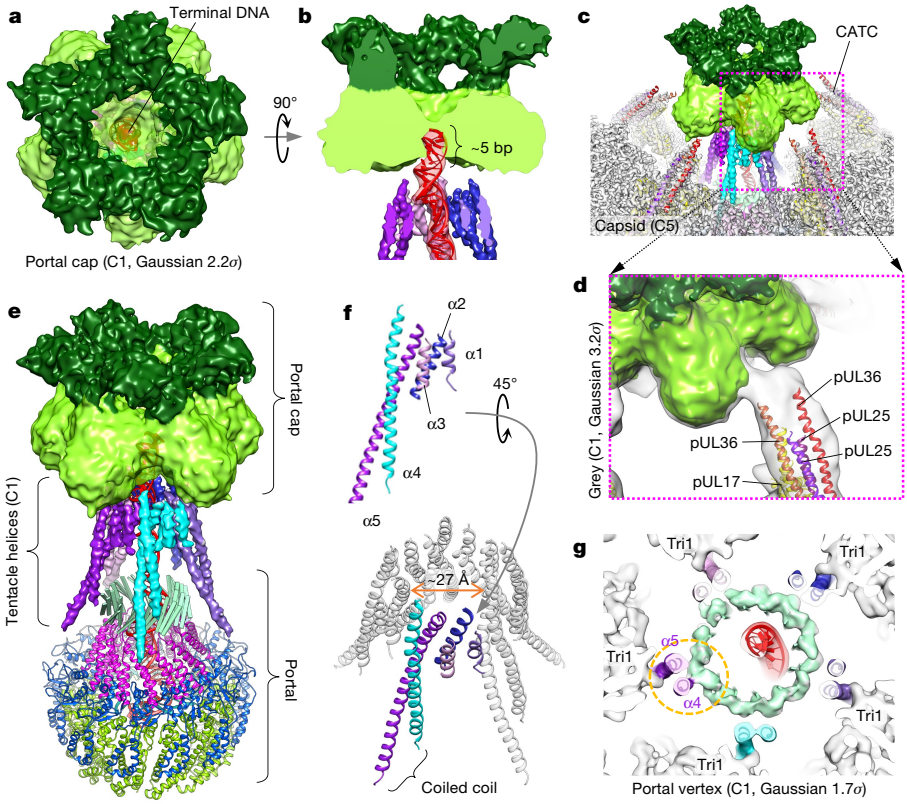

Fig. 3 | Tentacle helices and the portal cap. a, **b**, Axial view (**a**) and *z*-clipped side view (**b**) of the portal cap, which plugs the DNA translocation channel and interacts with terminal DNA. Shades of green emphasize the five dual lobes of the density (C1 portal vertex reconstruction, Gaussian-filtered to 2.2σ). **c**, Portal cap with surrounding capsid and CATC density (C5 portal vertex reconstruction) and CATC atomic models. **d**, Connecting density between portal cap and CATC helix bundles is visible in C1 density (portal vertex reconstruction) Gaussian-filtered to 3.2σ. **e**, Tentacle helices emanate upwards from the portal clip region, extending towards the portal cap. **f**, Poly-alanine models of tentacle helices. Five helices (α1–α5) constitute one set, and five sets encircle the DNA translocation channel. Helices α4 and α5 form a coiled-coil motif. **g**, Slab view, axial perspective of the portal clip region shows emerging α4 portal clip connecting density at lower thresholds (C1 portal vertex reconstruction, Gaussian-filtered to 1.7σ). Helix α5 also interacts with surrounding Tri1. See Supplementary Video 3.

C12 reconstruction, indicating flexibility and/or deviation from strict 12-fold symmetry. Although the full clip could not be modelled atomically, three β-strands visibly form a β-sheet in the clip above each monomer (Fig. 2e). Twelve sets of clip β-sheets give rise to a right-handed twisted-turret-like structure, forming the wall of an upper narrow region of the portal channel, approximately 33 Å across at its narrowest point, and where interactions with proximal toroidal DNA occur through the inner ring of β-strands (Fig. 2f). By contrast, β-hairpins are well-resolved in our C12 reconstruction, indicating a high degree of 12-fold symmetry. Each β-hairpin consists of two β-strands joined by an asparagine/glutamine-rich loop, which contacts distal toroidal DNA at several registers. Twelve β-hairpins extend perpendicularly towards the central axis of the portal channel, forming a disk-like structure with a central aperture about 30 Å in diameter that defines the narrowest point of the portal channel (Fig. 2g).

Unlike the clip and β-hairpin, the stem and wall domains do not contact terminal DNA. The stem helices give rise to a left-handed corkscrew structure just below the clip, a distinctive feature that is shared with phage portals[6] (Fig. 2c, Extended Data Fig. 5). In tandem, helix-rich stem and wall domains appear to form the structural framework on which the DNA-interacting clip and β-hairpin aperture are mounted. Indeed, force studies of the ϕ29 phage portal have demonstrated that these structural elements optimize the portal to withstand extreme mechanical stress, as might be imparted by translocating DNA[19]. Further evidence of the highly optimized structure of the portal is apparent in an electrostatic-surface rendering calculated from our model (Fig. 2h). In general, surfaces that interact with negatively charged DNA are positively charged. In particular, a chamber-like space beneath the portal aperture is strongly negatively charged and is likely to prevent interactions with newly translocated DNA that might otherwise affect proper genome compaction.

A pseudo-fivefold-symmetric portal cap emerges upon filtering our C1 portal vertex reconstruction (Fig. 3a). When aligned with terminal DNA, this portal cap appears to anchor the last five base pairs of the genome terminus (Fig. 3b). Notably, studies implicate pUL25 of CATC in several DNA–portal vertex-related capacities, including direct binding of DNA[20], DNA cleavage during packaging termination[20] and interaction with nuclear-pore complexes during viral genome uncoating[21,22]. Given that (1) five sets of pUL25 head-domain dimers form pentameric complexes above penton capsomers[23–25]; (2) the volume and five dual-lobed appearance of the portal cap density align with five pUL25 head dimers; and (3) connections between the portal cap and CATC helix bundles are visible at lower thresholds (Fig. 3c, d), consistent with the pUL25 head domain being flexibly linked[23,24]; we posit that the portal cap is a portal-vertex-specific configuration of five sets of pUL25 dimers, which plugs the DNA translocation channel upon dissolution of actively packaging terminase complex.

Visible in both C1 and C5 structures of the portal vertex, five sets of tentacle-like helix densities ring the DNA translocation channel, extending from the portal clip to the portal cap (Fig. 3e). Although they could not be modelled atomically, C_α bumps were sufficiently visible to permit polyalanine traces for each helix set. Each set consists of three short helices (α1–α3) and two long helices (α4–α5) arranged in a coiled coil (Fig. 3f). Gradually decreasing the threshold in our C1 portal vertex reconstruction reveals increasingly connected density between the portal clip and α4 (Fig. 3g). Given that the missing clip residues of the portal (residues 308–516) contain predicted long helical stretches interspersed with disordered residues (Extended Data

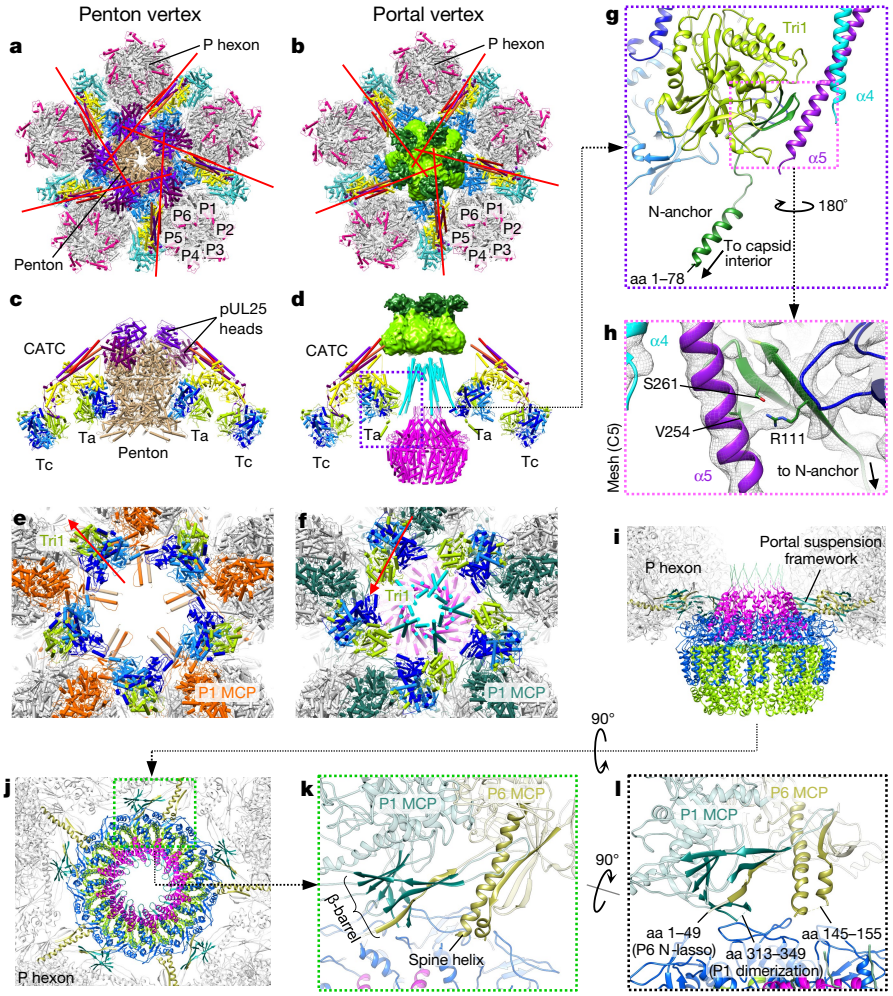

Fig. 4 | Capsid accommodations at the portal vertex. a, **b**, Axial views of penton vertex (**a**) and portal vertex (**b**). Pipe-and-plank models are coloured as follows: pUL17, yellow; pUL36c, red and orange; pUL25, cherry and purple; triplex Ta, blue; triplex Tc, teal. Red lines denote CATC helix bundle orientations. **c**, **d**, Side views of penton vertex (**c**) and portal vertex (**d**) structures. Triplexes are coloured: Tri1, lime; Tri2A, light blue; Tri2B, dark blue. **e**, **f**, Axial views of penton vertex with CATC and most of penton removed (**e**) and portal vertex with CATC/portal cap removed (**f**). Red arrows denote triplex orientations. Five penton dimerization domain helices forming 'star helix' interactions[23] with P1 MCPs are retained in **e**, exemplifying an alternate domain-level conformation. **g**, The Ta Tri1 capsid-penetrating N-anchor runs into a three-stranded β-sheet (dark green), which contacts α5 of the tentacle helices. **h**, Mesh density (C5 portal vertex reconstruction) shows interactions between α5 and Tri1 through Arg111 (also Val254 and Ser261 at lower thresholds). **i**, **j**, Side (**i**) and axial (**j**) views show the dodecameric portal suspended by five sets of β-barrels and spine helices from surrounding P hexons. **k**, Enlarged view of a β-barrel and spine helix motif. **l**, Flexible elements extend from the β-barrel and spine helix at the capsid-portal interface. See Supplementary Video 4. aa, amino acid.

Fig. 3)—in agreement with our density's strong but unconnected helical densities—we postulate that tentacle helices belong to unmodelled residues of the clip. While this interpretation necessitates an at-first-glance outlandish 12-to-5-fold symmetry reorganization within the portal structure, dodecameric procapsid portal in P22 phage is known to expose a 'quasi-fivefold symmetric surface' at the apex of its clip[26], where pentameric terminase presumably interfaces. Although the degree of fivefold symmetry in our tentacle helices exceeds that of the P22 procapsid portal, both examples underscore a tendency towards plasticity, which may be a requirement in a symmetry-mismatched interfacing region. Additionally, the association of the HSV-1 portal with terminase is known to require a leucine zipper in the unmodelled region of the pUL6 clip[27].

Finally, using our C5 reconstruction, we built atomic models of periportal small capsid protein (SCP)-decorated P hexon, Ta and Tc triplex and CATC, enabling direct comparison of penton[23] and portal vertices (Supplementary Video 4). Portal-specific structures aside—that is, portal, tentacle helices and portal cap—periportal CATC helix bundles are visibly oriented more perpendicularly to the central axis of the vertex (Fig. 4a, b), perhaps to facilitate a portal-vertex-specific configuration of pUL25 head dimers required to form the portal cap. Furthermore, periportal Ta triplexes are rotated approximately 120° anticlockwise about their respective centres, relative to peripenton Ta (Fig. 4c–f), such that the capsid-penetrating N-anchor of periportal Ta Tri1 (of which an additional 24 residues are visible versus that of peripenton Ta Tri1; Extended Data Fig. 6) is brought into direct contact with α5 of the tentacle helices through Tri1 Arg111 (Fig. 4g, h). Our models also reveal a repurposing of major capsid protein (MCP) N-lasso and dimerization domains[23] in the periportal floor, facilitating a 'rigid framework-flexible contact' strategy to accommodate the symmetry-mismatched pseudo-fivefold-symmetric capsid and dodecameric portal (Fig. 4i, j, Extended Data Fig. 6). This rearrangement results in five sets of β-barrels occupying five portal-surrounding registers, which, together with five corresponding MCP spine helices, provide a structured framework from which short, flexible MCP elements extend to interface with the loop-rich wing domains of the portal (Fig. 4k, l).

This work thus resolves previously averaging-obscured structures of the HSV-1 portal vertex and reveals an accommodation of symmetry mismatches through both intermolecular and intramolecular plasticity. Notably, the projection of tentacle helices from the portal clip towards the terminase docking site or portal cap and the coiled-coil arrangement of α4 and α5 (coiled-coil motifs are widely implicated in

propagating conformation changes[28]) are evocative of a signalling pathway. In light of evidence of sequence- and headful-sensing regulatory effects in genome packaging[17,18,29,30], the interaction of α4 with the DNA-interacting region of the portal clip and of α5 with the probe-like, capsid-penetrating N-anchor of Tri1 suggest possible mechanistic bases for these modes of regulation of genome packaging.

Online content

Any Methods, including any statements of data availability and Nature Research reporting summaries, along with any additional references and Source Data files, are available in the online version of the paper at https://doi.org/10.1038/s41586-019-1248-6.

Received: 5 June 2018; Accepted: 26 April 2019;
Published online: 29 May 2019

1. Bauer, D. W., Huffman, J. B., Homa, F. L. & Evilevitch, A. Herpes virus genome, the pressure is on. *J. Am. Chem. Soc.* **135**, 11216–11221 (2013).
2. Zhou, Z. H. et al. Seeing the herpesvirus capsid at 8.5 Å. *Science* **288**, 877–880 (2000).
3. Yu, X. K., Jih, J., Jiang, J. S. & Zhou, Z. H. Atomic structure of the human cytomegalovirus capsid with its securing tegument layer of pp150. *Science* **356**, eaam6892 (2017).
4. Heming, J. D., Huffman, J. B., Jones, L. M. & Homa, F. L. Isolation and characterization of the herpes simplex virus 1 terminase complex. *J. Virol.* **88**, 225–236 (2014).
5. Neuber, S. et al. Mutual Interplay between the human cytomegalovirus terminase subunits pUL51, pUL56, and pUL89 promotes terminase complex formation. *J. Virol.* **91**, e02384-16 (2017).
6. Rao, V. B. & Feiss, M. Mechanisms of DNA Packaging by large double-stranded DNA viruses. *Annu. Rev. Virol.* **2**, 351–378 (2015).
7. Tang, J. et al. DNA poised for release in bacteriophage ϕ29. *Structure* **16**, 935–943 (2008).
8. Mao, H. et al. Structural and molecular basis for coordination in a viral DNA packaging motor. *Cell Reports* **14**, 2017–2029 (2016).
9. Harjes, E. et al. Structure of the RNA claw of the DNA packaging motor of bacteriophage Φ29. *Nucleic Acids Res.* **40**, 9953–9963 (2012).
10. Jiang, W. et al. Structure of epsilon15 bacteriophage reveals genome organization and DNA packaging/injection apparatus. *Nature* **439**, 612–616 (2006).
11. Booy, F. P. et al. Liquid-crystalline, phage-like packing of encapsidated DNA in herpes simplex virus. *Cell* **64**, 1007–1015 (1991).
12. Newcomb, W. W., Cockrell, S. K., Homa, F. L. & Brown, J. C. Polarized DNA ejection from the herpesvirus capsid. *J. Mol. Biol.* **392**, 885–894 (2009).
13. Ray, K., Ma, J., Oram, M., Lakowicz, J. R. & Black, L. W. Single-molecule and FRET fluorescence correlation spectroscopy analyses of phage DNA packaging: colocalization of packaged phage T4 DNA ends within the capsid. *J. Mol. Biol.* **395**, 1102–1113 (2010).
14. Mocarski, E. S. & Roizman, B. Structure and role of the herpes simplex virus DNA termini in inversion, circularization and generation of virion DNA. *Cell* **31**, 89–97 (1982).
15. Tong, L. & Stow, N. D. Analysis of herpes simplex virus type 1 DNA packaging signal mutations in the context of the viral genome. *J. Virol.* **84**, 321–329 (2010).
16. Umene, K. Cleavage in and around the DR1 element of the A sequence of herpes simplex virus type 1 relevant to the excision of DNA fragments with length corresponding to one and two units of the A sequence. *J. Virol.* **75**, 5870–5878 (2001).
17. McVoy, M. A., Nixon, D. E., Adler, S. P. & Mocarski, E. S. Sequences within the herpesvirus-conserved pac1 and pac2 motifs are required for cleavage and packaging of the murine cytomegalovirus genome. *J. Virol.* **72**, 48–56 (1998).
18. Wang, J. B., Nixon, D. E. & McVoy, M. A. Definition of the minimal *cis*-acting sequences necessary for genome maturation of the herpesvirus murine cytomegalovirus. *J. Virol.* **82**, 2394–2404 (2008).
19. Kumar, R. & Grubmüller, H. Elastic properties and heterogeneous stiffness of the phi29 motor connector channel. *Biophys. J.* **106**, 1338–1348 (2014).
20. Ogasawara, M., Suzutani, T., Yoshida, I. & Azuma, M. Role of the UL25 gene product in packaging DNA into the herpes simplex virus capsid: location of UL25 product in the capsid and demonstration that it binds DNA. *J. Virol.* **75**, 1427–1436 (2001).
21. Huffman, J. B. et al. The C terminus of the herpes simplex virus UL25 protein is required for release of viral genomes from capsids bound to nuclear pores. *J. Virol.* **91**, e00641-17 (2017).
22. Pasdeloup, D., Blondel, D., Isidro, A. L. & Rixon, F. J. Herpesvirus capsid association with the nuclear pore complex and viral DNA release involve the nucleoporin CAN/Nup214 and the capsid protein pUL25. *J. Virol.* **83**, 6610–6623 (2009).
23. Dai, X. & Zhou, Z. H. Structure of the herpes simplex virus 1 capsid with associated tegument protein complexes. *Science* **360**, eaao7298 (2018).
24. Liu, Y. T. et al. A pUL25 dimer interfaces the pseudorabies virus capsid and tegument. *J. Gen. Virol.* **98**, 2837–2849 (2017).
25. Wang, J. et al. Structure of the herpes simplex virus type 2 C-capsid with capsid-vertex-specific component. *Nat. Commun.* **9**, 3668 (2018).
26. Lokareddy, R. K. et al. Portal protein functions akin to a DNA-sensor that couples genome-packaging to icosahedral capsid maturation. *Nat. Commun.* **8**, 14310 (2017).
27. Yang, K., Wills, E. & Baines, J. D. The putative leucine zipper of the UL6-encoded portal protein of herpes simplex virus 1 is necessary for interaction with pUL15 and pUL28 and their association with capsids. *J. Virol.* **83**, 4557–4564 (2009).
28. Truebestein, L. & Leonard, T. A. Coiled-coils: the long and short of it. *BioEssays* **38**, 903–916 (2016).
29. Rao, V. B. & Black, L. W. *DNA Packaging in Bacteriophage T4 in Viral Genome Packaging Machines* (Plenum, 2005).
30. Berndsen, Z. T., Keller, N. & Smith, D. E. Continuous allosteric regulation of a viral packaging motor by a sensor that detects the density and conformation of packaged DNA. *Biophys. J.* **108**, 315–324 (2015).

Acknowledgements We thank W. Liu for assistance in molecular dynamic flexible fitting. This research has been supported in part by grants from the National Key R&D Program of China (2017YFA0505300 and 2016YFA0400900) and the US National Institutes of Health (GM071940/DE025567/DE028583/AI094386). We acknowledge the use of instruments at the Electron Imaging Center for Nanomachines supported by UCLA and by instrumentation grants from NIH (1S10RR23057 and 1U24GM116792) and NSF (DBI-1338135 and DMR-1548924). We thank the Bioinformatics Center of the University of Science and Technology of China, School of Life Science, for providing supercomputing resources for this project.

Reviewer information *Nature* thanks Sarah Butcher, Venigalla Rao and the other anonymous reviewer(s) for their contribution to the peer review of this work.

Author contributions Z.H.Z. conceived the project; Z.H.Z. and G.-Q.B. supervised research; X.D. recorded the data; Y.-T.L. processed the data; J.J. built atomic models and made illustrations and videos; Z.H.Z., J.J. and Y.-T.L. analysed the results and wrote the paper. All authors edited and approved the paper.

Competing interests The authors declare no competing interests.

Additional information
Extended data is available for this paper at https://doi.org/10.1038/s41586-019-1248-6.
Supplementary information is available for this paper at https://doi.org/10.1038/s41586-019-1248-6.
Reprints and permissions information is available at http://www.nature.com/reprints.
Correspondence and requests for materials should be addressed to Z.H.Z.
Publisher's note: Springer Nature remains neutral with regard to jurisdictional claims in published maps and institutional affiliations.

METHODS

Cryo-EM sample preparation and imaging. Sample preparation (HSV-1 virion) and cryo-EM imaging have been described previously[23]. In brief, virions of HSV-1 strain KOS were purified with density gradient centrifugation and frozen for cryo-EM imaging. About 8,000 movies were collected with Leginon[31] in a Titan Krios with energy filter and K2 direct electron detector. Each movie stack was drift-corrected[32] and averaged to produce a corresponding micrograph. Defocus values for each micrograph were determined with CTFFIND3[33] and found to be in the range of −1 μm to −3 μm. A total of 45,445 particles (1,440 × 1,440 pixels and 1.03 Å per pixel) were picked manually with the boxer program in EMAN[34] and boxed out from the micrographs with relion_preprocess in Relion[35].

Icosahedral reconstruction and vertex sub-particle extraction. At 1,440 × 1,440 pixels per individual particle image, the dataset required an unrealistic amount of computational resources and was too large to process with Relion. Thus, particles were binned four times using relion_preprocess and submitted for autorefinement with Relion2.1[35,36] imposing I3 symmetry. A Gaussian ball was used as an initial reference of the icosahedral reconstruction.

To perform symmetry relaxation, we expanded the icosahedral symmetry of the particles using relion_particle_symmetry_expand, generating 60 orientations for each particle. Each orientation has three Euler angles denoted as parameters within the Relion star files: rot (_rlnAngleRot), tilt (_rlnAngleTilt) and psi (_rlnAnglePsi). We then selected 12 orientations of 12 vertices from the 60 icosahedrally related orientations as follows. First, we noted that because the icosahedral reconstruction was performed using I3 symmetry, there are five redundant orientations relative to each vertex that differ only in their rot angles (the first angle rotated about the *z*-axis). Given this observation, we then assigned 60 orientations into 12 groups with 5 orientations in each group. Importantly, the orientations within a group each have different rot angles, but the same tilt and psi angles. Lastly, we selected one orientation in each group as the orientation of a vertex, thereby generating one orientation for each vertex out of the 60 icosahedral-related orientations.

Previous study showed sub-particle reconstruction could solve structures of symmetry-mismatched parts of macromolecular complexes[37]. We then sought to extract sub-particles containing only vertices from the unbinned virion particles based upon the unique orientations previously selected. To do so, the two-dimensional Cartesian positions (x, y) of each sub-particle on their respective particle images were calculated using the following formula:

$$\begin{cases} x = \cos(\text{psi})\sin(\text{tilt})d + C - O_x \\ y = -\sin(\text{psi})\sin(\text{tilt})d + C - O_y \end{cases} \quad (1)$$

where d is the distance from the centre of the reconstructed capsid to the vertex (in our case, $d = 567$ pixels) and C is the centre of the two-dimensional projection image (in our case, the projection centre is at (720, 720), so $C = 720$ pixels). Because icosahedral reconstruction was performed with four times-binned particles, O_x and O_y are four times the offset distance (_rlnOriginX and _rlnOriginY in Relion) of each particle image relative to the projection centre of the icosahedral reconstruction. Finally, sub-particles (384 × 384 pixels) containing only vertices, henceforth termed 'vertex sub-particles', were extracted from particle images based on their calculated positions using relion_preprocess without further normalization.

The resolution of the enormous virus particles was largely limited by the well-documented depth-of-focus problem[38,39]. To overcome this limitation, the defocus value of each vertex sub-particle was calculated on the basis of their locations with the following formula, where Δz_0 is the original defocus and Δz is the new defocus for each vertex:

$$\Delta z = \Delta z_0 - \cos(\text{tilt})d \quad (2)$$

Classification and refinement of vertex sub-particles with fivefold symmetry. To classify the portal vertex from the 12 vertices of each virus, we used Relion2.1 to perform three-dimensional classification without rotational search (only ±4 pixels offset search) on the extracted vertex sub-particle, using the predetermined orientation of vertices while imposing fivefold symmetry. The initial reference for classification was a 30 Å reconstruction of the vertex sub-particles using relion_reconstruct. After 29 iterations, four classes were generated through three-dimensional classification. One of the four classes exhibited apparent structural differences compared to the rest of the classes, which we deemed a portal vertex. This class contained 7.9% (~1/12) of the vertex sub-particles, consistent with exactly 1 out of 12 capsid vertices being a portal vertex. In rare cases, more than one vertex from each capsid was classified into the portal vertex class, probably owing to the low quality of these particles and/or errors in classification. These redundant particles were removed according to the following criteria: if two or more vertices from the same virus particle were assigned to the portal vertex class, only the vertex sub-particle with the highest _rlnMaxValueProbDistribution score was retained. Upon removing all redundant particles, 42,857 vertex sub-particles remained and were deemed sub-particles of the portal vertex, henceforth referred to as 'portal vertex sub-particles'. Three-dimensional autorefinement with imposed fivefold symmetry was then performed on these portal vertex sub-particles with only a local search for orientation determination. The final resolution of the reconstruction was estimated with two independently refined maps from halves of the dataset with gold-standard Fourier shell correlation (FSC) at the 0.143 criterion[40] using relion_postprocess, and determined to be 4.3 Å (Extended Data Fig. 2a). This reconstruction of the portal vertex contains a well-resolved fivefold-arranged capsid, tegument, and fivefold-symmetric DNA packaging-related structures, but a smeared portal dodecamer density owing to symmetry mismatch.

Reconstructing the pUL6 dodecameric portal with 12-fold symmetry. In the portal vertex sub-particles, we can further extract sub-particles that contain only the pUL6 dodecamer in order to reconstruct the 12-fold symmetric portal. The positions of pUL6 dodecamer on portal vertex sub-particles were determined using equation (1). The Euler angles (rot, tilt and psi), O_x, and O_y are the orientation parameters of the portal vertex sub-particles; d is the distance from the centre of the dodecamer to the centre of the portal vertex sub-particle reconstruction (−126 pixels); and C is the centre of two-dimensional projection image of the portal vertex sub-particle (192 pixels). The sub-particles of pUL6 dodecamer (192 × 192 pixels), henceforth referred to as 'dodecamer sub-particles' were then extracted with relion_preprocess using these parameters.

To obtain a reconstruction of the pUL6 dodecamer, we first expanded the fivefold symmetry of the dodecamer sub-particles using relion_particle_symmetry_expand, generating five unique orientations for each dodecamer sub-particle. We then applied three-dimensional classification with imposed C12 symmetry without orientation search, which after 100 iterations yielded five classes of similar structures with a rotational difference of approximately 72° in between classes. Ideally, each of the five expanded orientations of each dodecamer sub-particle should be assigned to exactly one of the five classes such that each class should contain 20% of the symmetry expanded sub-particles. After removing redundant particles as previously described—only particles with the highest _rlnMaxValueProbDistribution score were retained—the five classes contained 32,975; 39,939; 38,694; 36,102 and 34,722 particles, respectively. Since the five reconstructed classes were of the same quality upon visual inspection, we chose the class with the most abundant particles for three-dimensional refinement with imposed 12-fold symmetry and limited to local orientation search. As before, the resolution of the pUL6 dodecamer was determined with relion_postprocess using gold-standard FSC at the 0.143 criterion[40] (Extended Data Fig. 2a), indicating an overall resolution of approximately 5.6 Å for our 12-fold-symmetric reconstruction. However, a visual assessment of the region's density quality and the local resolution estimate from ResMap[41] indicates the majority of the portal itself to be within the 4–5 Å resolution range (Extended Data Fig. 2e), thereby allowing ab initio modelling. The lower resolution estimated by FSC may be due to unresolved, fairly flexible regions of the portal as well as other protein and nucleic acid densities that deviate from proper 12-fold symmetry.

Asymmetric reconstruction of the portal vertex and virion. As the orientations determined from the previous classification of pUL6 dodecamer were selected from one of the five expanded orientations, these orientations can be used for three-dimensional refinement of the portal vertex and whole virion without symmetry. Owing to the large computational requirement for refinement of the whole virion, we performed this refinement using two-times binned particles. The asymmetric autorefinement for both portal vertex sub-particles and virion particles were performed with a local search for orientations determined from the classification of the pUL6 dodecamer. The resolution of the portal vertex complex and the whole virion as determined by relion_postprocess are 5.4 Å and 6.2 Å, respectively (Extended Data Fig. 2a), according to the gold-standard FSC at 0.143 criterion[40].

Asymmetric reconstruction of terminal DNA. Despite obtaining an asymmetric reconstruction of the portal vertex structure with well-resolved high-resolution features, the terminal DNA within the portal channel remained smeared. Given that terminal DNA interacts with the portal, it could occupy any one of the twelve equivalent registers of the portal channel and the smeared DNA density is probably a result of undistinguished orientations of the terminal DNA among twelve possibilities.

To determine terminal DNA structure, we further expanded the orientations determined during the asymmetric portal vertex reconstruction with 12-fold symmetry using relion_particle_symmetry_expand. A cylindrical mask with a radius of 1.8 nm and a length of 18.5 nm encompassing the inner portal channel region was generated to facilitate three-dimensional masked classification, which was performed without orientation search on the symmetry-expanded portal vertex particles (384 × 384 pixels). To enhance the signal-to-noise ratios of the classified structures, we classified the particles into six rather than twelve classes, setting the tau factor in Relion[42] to 80, given the small size of the mask region. After 72 iterations of classification, six classes were generated, from which we chose the class with the best structure of continuous DNA density. Redundant particles from this class were removed as previously described, after which we performed three-dimensional refinement with local searching for orientations and with a mask

covering both the portal and terminal DNA. Using relion_postprocess, we determined the resolution of our terminal DNA reconstruction to be 10.1 Å (Extended Data Fig. 2b), once again according to the gold-standard FSC at 0.143 criterion[40].

Atomic modelling of capsid, CATC and portal proteins. Atomic models of peripenton (that is, non-portal vertex adjacent) MCP, Tri1, Tri2A, Tri2B, SCP, pUL17, pUL25 and pUL36 have been described previously[23]. Using our C5 map of the portal vertex region, we docked in peripenton copies of the SCP-decorated P hexon, Ta triplex, and CATC in Chimera[43]. We then refined these models as necessary based on our density maps using the crystallographic program COOT[44] to produce portal-vertex-specific atomic models. Notably, periportal P1 and P6 MCP demonstrated substantial deviation from their peripenton counterparts in the MCP floor and required full re-traces in some regions. Periportal Ta triplex also exhibited a different orientation than peripenton Ta triplex, requiring manual rebuilding of some loop and interfacing regions. Periportal capsid and CATC models were then improved using real space refinement in Phenix[45]. Subsequent iterations of manual refinement in COOT and real space refinement in Phenix were applied to optimize the atomic models.

We traced and atomically modelled the pUL6 dodecameric portal ab initio using the C12 symmetry map and with the aid of secondary structure predictions obtained from Phyre2[46]. Homologues of HSV-1 pUL6 from enterobacteria phage P22 (Protein Data Bank (PDB) IDs 5JJ1 and 5JJ3), bacteriophage SPP1 (PDB 2JES) and bacteriophage T4 (PDB 3JA7) were also used to help to determine the correct trace (Extended Data Fig. 5). Side-chain densities were consistently visible in the C12 map and served as reliable markers during registration; manually built models were then refined with real space refinement in Phenix. Final post-refinement validation statistics for all atomic models are tabulated in Extended Data Table 1. As we were unable to definitively identify the proteins that constituted the tentacle helices observed in between the dodecameric portal and portal cap, we were unable to register amino acid sequences for these densities. However, we built polyalanine helices into these densities using observable C_α bumps through the C-alpha_Baton_Mode and Ca_Zone->Mainchain utilities in COOT.

Flexible fitting of terminal DNA. To model the terminal DNA within the portal channel, we first generated a relaxed, straight segment of double-stranded B-form DNA with 90 repeating cytosine base pairs using the Ideal_DNA/RNA utility in COOT. After rigid body-fitting our ideal dsDNA into our asymmetric reconstruction of terminal DNA, we used Chimera[43] to mask out density beyond the central cylindrical region of the portal channel. The resulting map and 90-bp ideal dsDNA model were then submitted to a molecular dynamics flexible fitting (MDFF)[47] simulation session to flexibly fit the ideal dsDNA into the density map. Using the resulting dsDNA atomic model with improved density map fit, we determined that the length of visible dsDNA within the portal channel was approximately 67 bp long. Given that the last-packaged terminal DNA base pair must be oriented most distal from the capsid interior, we assigned this 67-bp long sequence to the last 67 bp of the HSV-1 concatemer and truncated and mutated our flexibly-fit dsDNA model accordingly. After manually adding an overhanging cytosine at the distal 3′ end (adjacent to the portal cap) as consistent with the concatemeric cleavage site, we used Color_Zone in Chimera[43] to segment out a more accurate DNA density from our asymmetric terminal DNA reconstruction. This improved segmented map and our modified 67-bp model were then submitted for a second round of MDFF simulation to obtain our final terminal DNA model.

Reporting summary. Further information on research design is available in the Nature Research Reporting Summary linked to this paper.

Data availability

The five cryo-EM maps have been deposited in the Electron Microscopy Data Bank (EMDB) under accession numbers EMD-9860 (C5 portal vertex reconstruction), EMD-9861 (C1 portal vertex reconstruction), EMD-9862 (C12 portal reconstruction), EMD-9863 (C1 terminal DNA and portal vertex reconstruction) and EMD-9864 (C1 virion reconstruction). The atomic models for pUL6 and periportal capsid or CATC proteins have been deposited in the Protein Data Bank under accession numbers 6OD7 and 6ODM, respectively.

31. Suloway, C. et al. Automated molecular microscopy: the new Leginon system. *J. Struct. Biol.* **151**, 41–60 (2005).
32. Li, X. M. et al. Electron counting and beam-induced motion correction enable near-atomic-resolution single-particle cryo-EM. *Nat. Methods* **10**, 584–590 (2013).
33. Mindell, J. A. & Grigorieff, N. Accurate determination of local defocus and specimen tilt in electron microscopy. *J. Struct. Biol.* **142**, 334–347 (2003).
34. Ludtke, S. J., Baldwin, P. R. & Chiu, W. EMAN: semiautomated software for high-resolution single-particle reconstructions. *J. Struct. Biol.* **128**, 82–97 (1999).
35. Scheres, S. H. W. RELION: implementation of a Bayesian approach to cryo-EM structure determination. *J. Struct. Biol.* **180**, 519–530 (2012).
36. Scheres, S. H. W. A Bayesian view on cryo-EM structure determination. *J. Mol. Biol.* **415**, 406–418 (2012).
37. Ilca, S. L. et al. Localized reconstruction of subunits from electron cryomicroscopy images of macromolecular complexes. *Nat. Commun.* **6**, 8843 (2015).
38. DeRosier, D. J. Correction of high-resolution data for curvature of the Ewald sphere. *Ultramicroscopy* **81**, 83–98 (2000).
39. Zhang, X. & Zhou, Z. H. Limiting factors in atomic resolution cryo electron microscopy: no simple tricks. *J. Struct. Biol.* **175**, 253–263 (2011).
40. Rosenthal, P. B. & Henderson, R. Optimal determination of particle orientation, absolute hand, and contrast loss in single-particle electron cryomicroscopy. *J. Mol. Biol.* **333**, 721–745 (2003).
41. Kucukelbir, A., Sigworth, F. J. & Tagare, H. D. Quantifying the local resolution of cryo-EM density maps. *Nat. Methods* **11**, 63–65 (2014).
42. Scheres, S. H. Processing of structurally heterogeneous cryo-EM data in RELION. *Methods Enzymol.* **579**, 125–157 (2016).
43. Pettersen, E. F. et al. UCSF Chimera—a visualization system for exploratory research and analysis. *J. Comput. Chem.* **25**, 1605–1612 (2004).
44. Emsley, P., Lohkamp, B., Scott, W. G. & Cowtan, K. Features and development of Coot. *Acta Crystallogr. D* **66**, 486–501 (2010).
45. Adams, P. D. et al. PHENIX: a comprehensive Python-based system for macromolecular structure solution. *Acta Crystallogr. D* **66**, 213–221 (2010).
46. Kelley, L. A., Mezulis, S., Yates, C. M., Wass, M. N. & Sternberg, M. J. E. The Phyre2 web portal for protein modeling, prediction and analysis. *Nat. Protoc.* **10**, 845–858 (2015).
47. Trabuco, L. G., Villa, E., Mitra, K., Frank, J. & Schulten, K. Flexible fitting of atomic structures into electron microscopy maps using molecular dynamics. *Structure* **16**, 673–683 (2008).

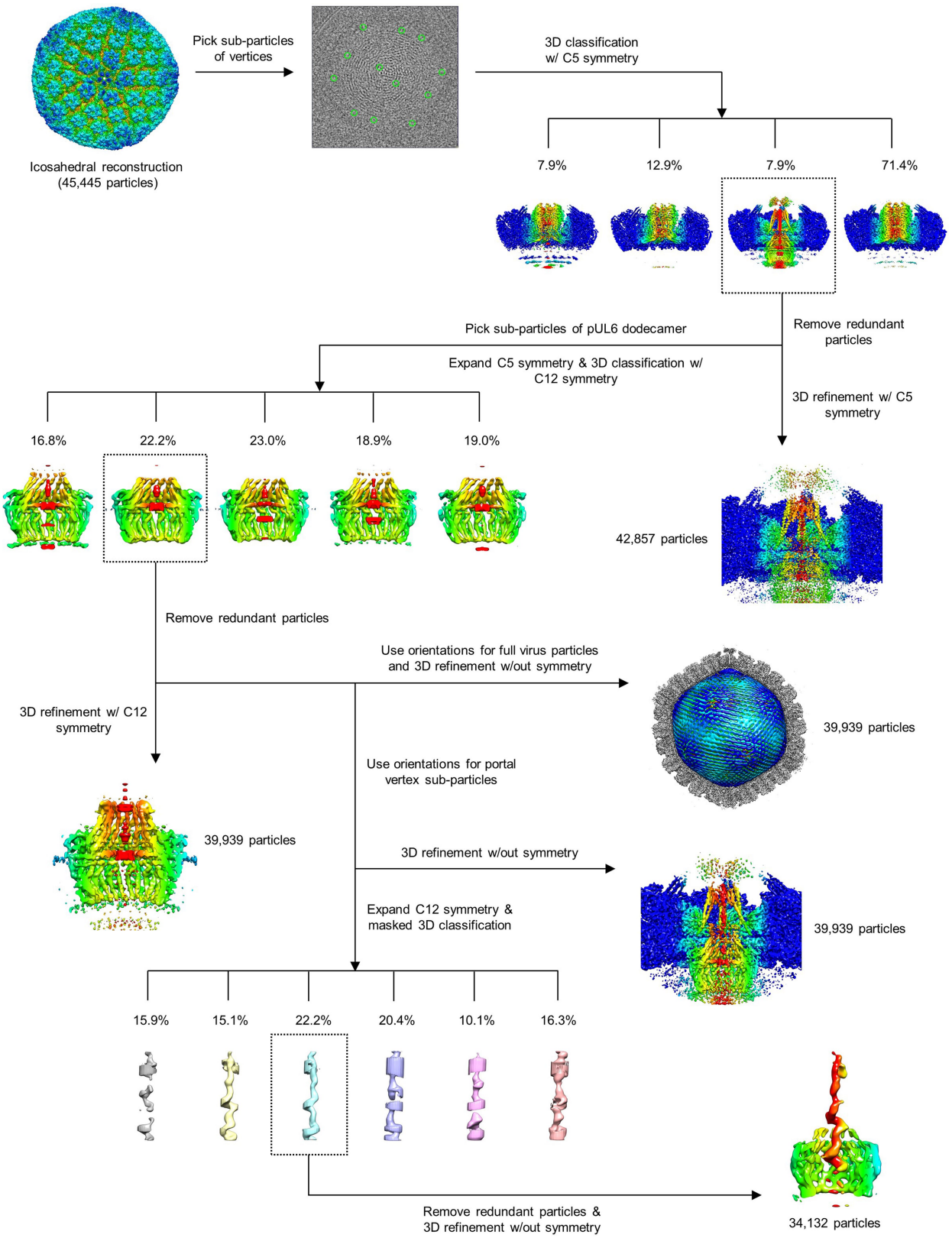

Extended Data Fig. 1 | Sequential localized classification and sub-particle reconstruction. Flow chart illustrates the identification and resolution of symmetry-mismatched structures of the unique portal vertex.

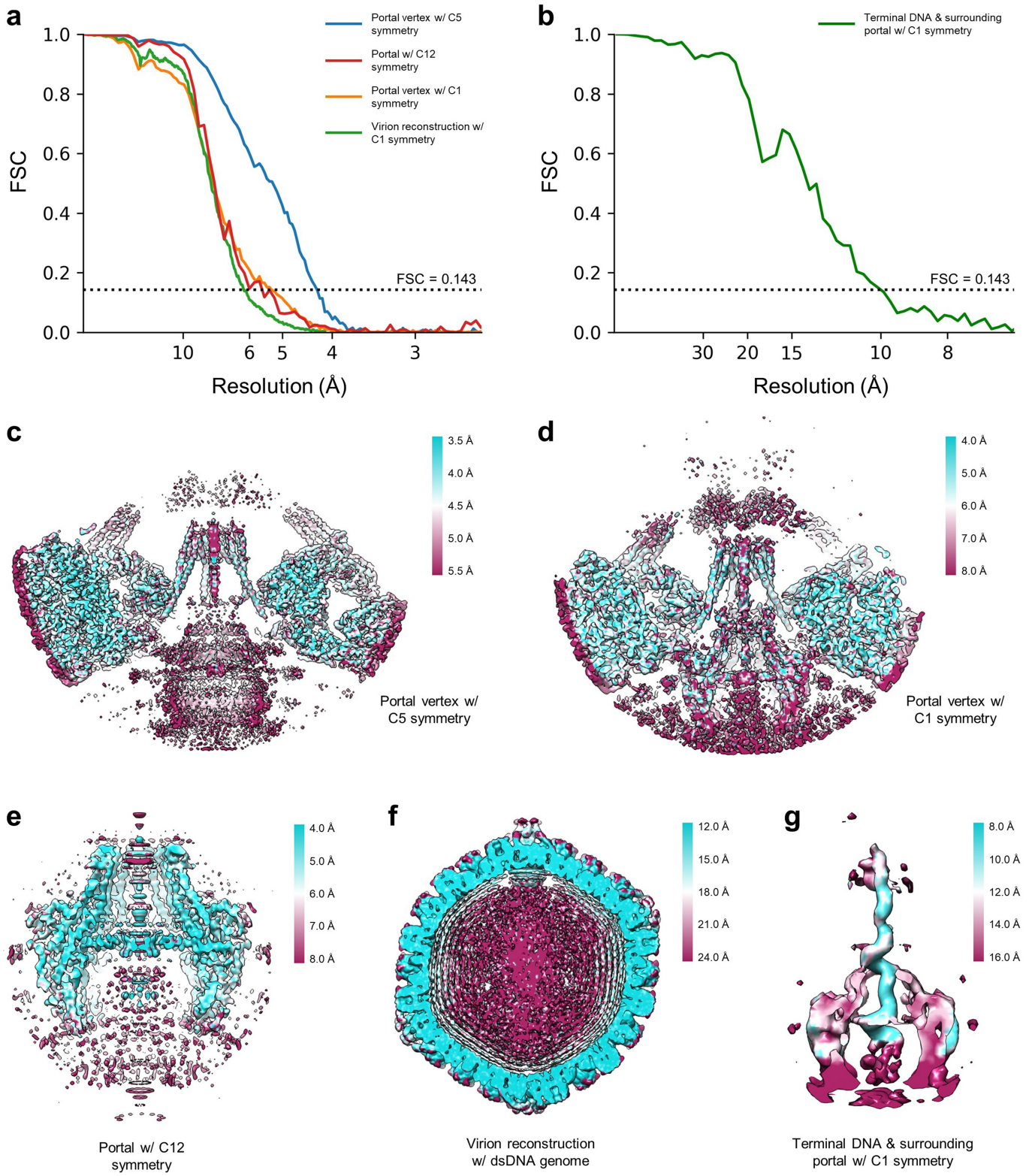

Extended Data Fig. 2 | Resolution verification. a, **b**, Resolution of reconstructions determined by gold-standard FSC at the 0.143 criterion. **c**–**g**, Density slices coloured by local resolution estimated from ResMap[41].

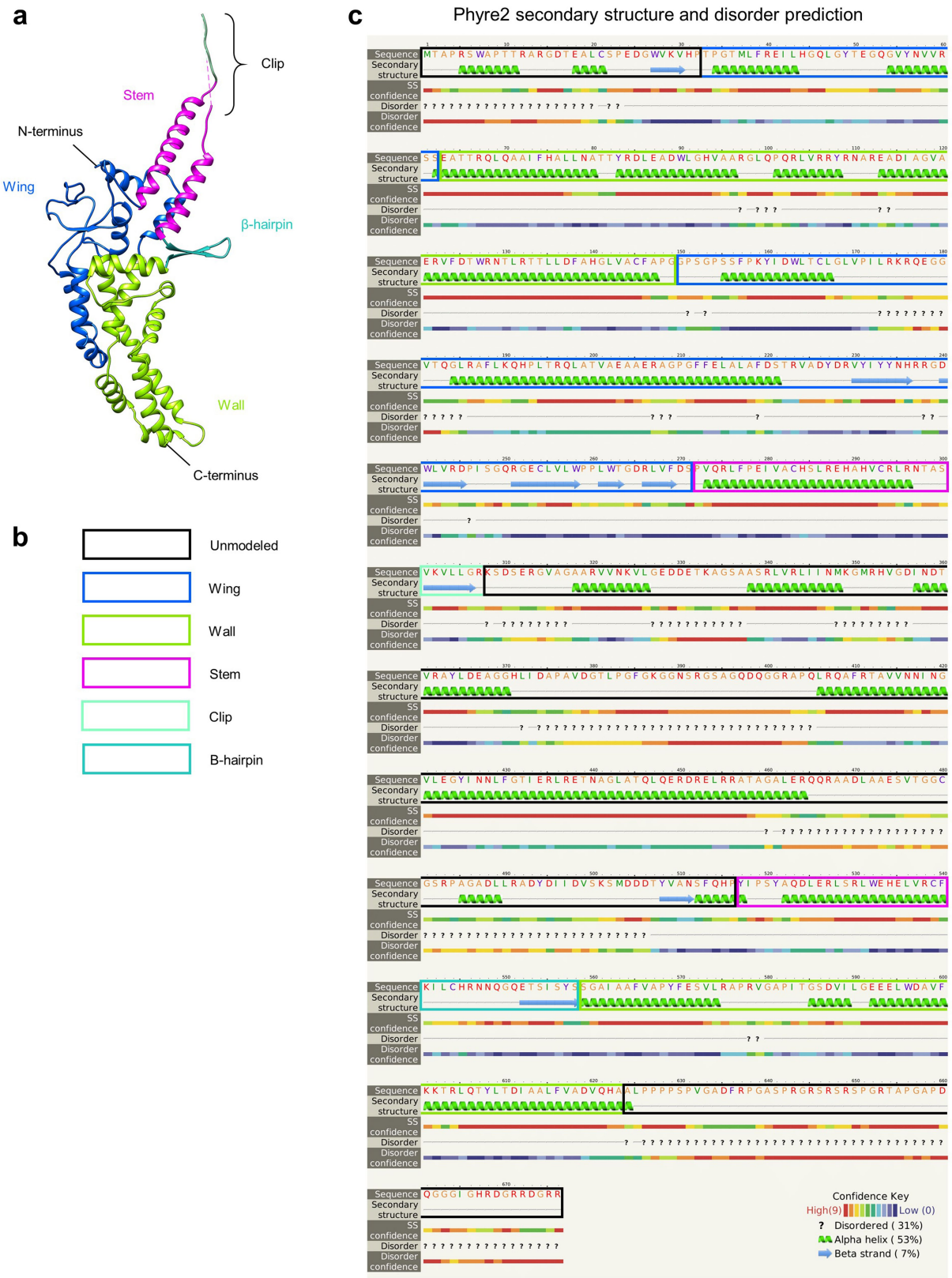

Extended Data Fig. 3 | pUL6 secondary structure and disorder prediction. **a**–**c**, pUL6 monomer coloured by domain for reference (**a**) and key (**b**) used to annotate a secondary structure and disorder prediction of pUL6 amino acid sequence (**c**) obtained from Phyre2[46].

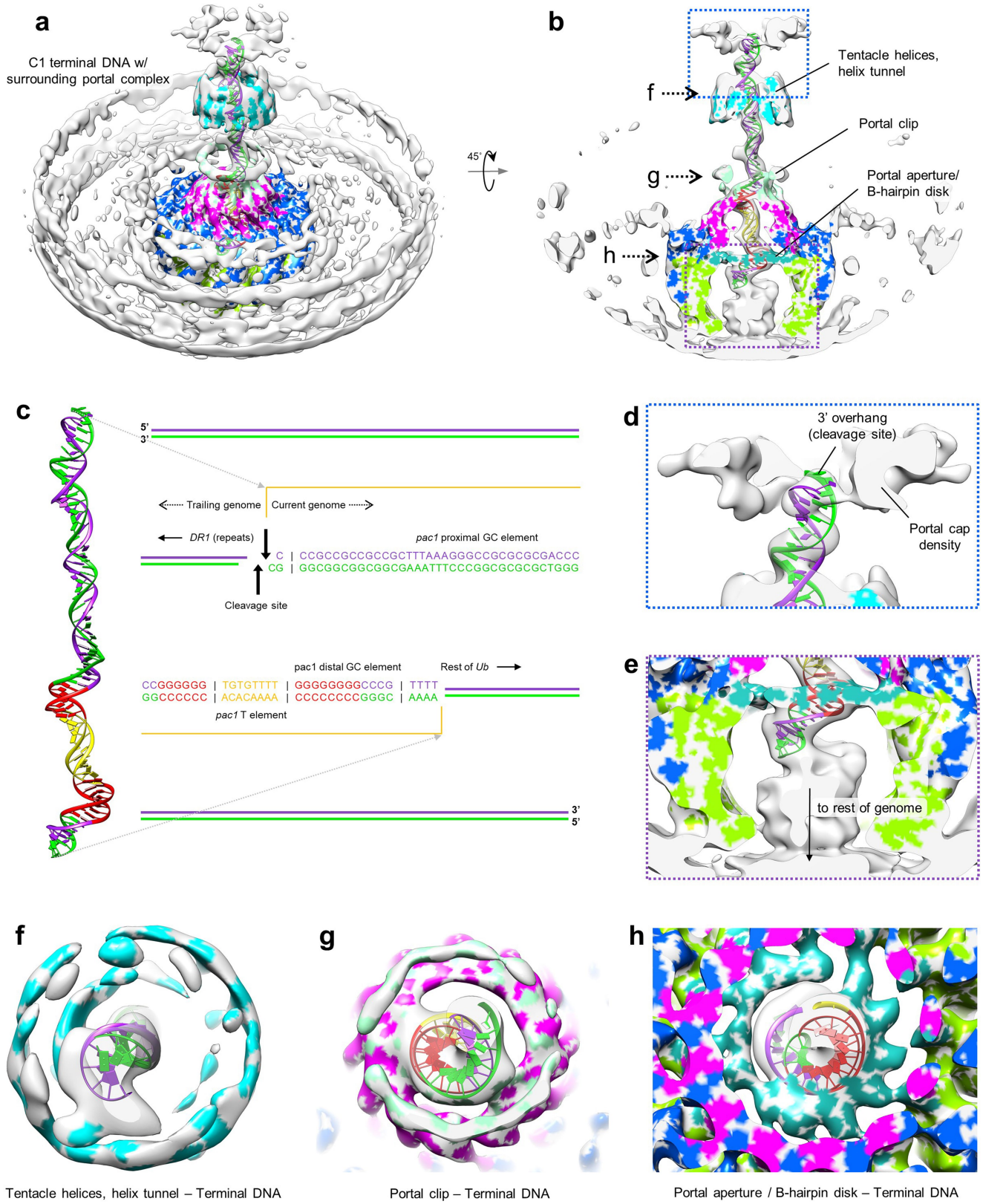

Extended Data Fig. 4 | Reconstruction of terminal DNA with surrounding portal. a, **b**, C1 reconstruction of terminal DNA with surrounding portal colour-zoned by pUL6 domains and tentacle helices. **c**, Sequence of terminal DNA mapped onto our fitted terminal DNA model. **d**, Enlarged view of the trailing end of terminal DNA, where concatemeric cleavage occurs. **e**, Enlarged view of terminal the disordered leading end of DNA, which extends down through the portal aperture towards the interior of the capsid. **f**–**h**, Slab views of C1 density showing interaction of terminal DNA with tentacle helices (**f**), portal clip (**g**) and the portal aperture (**h**).

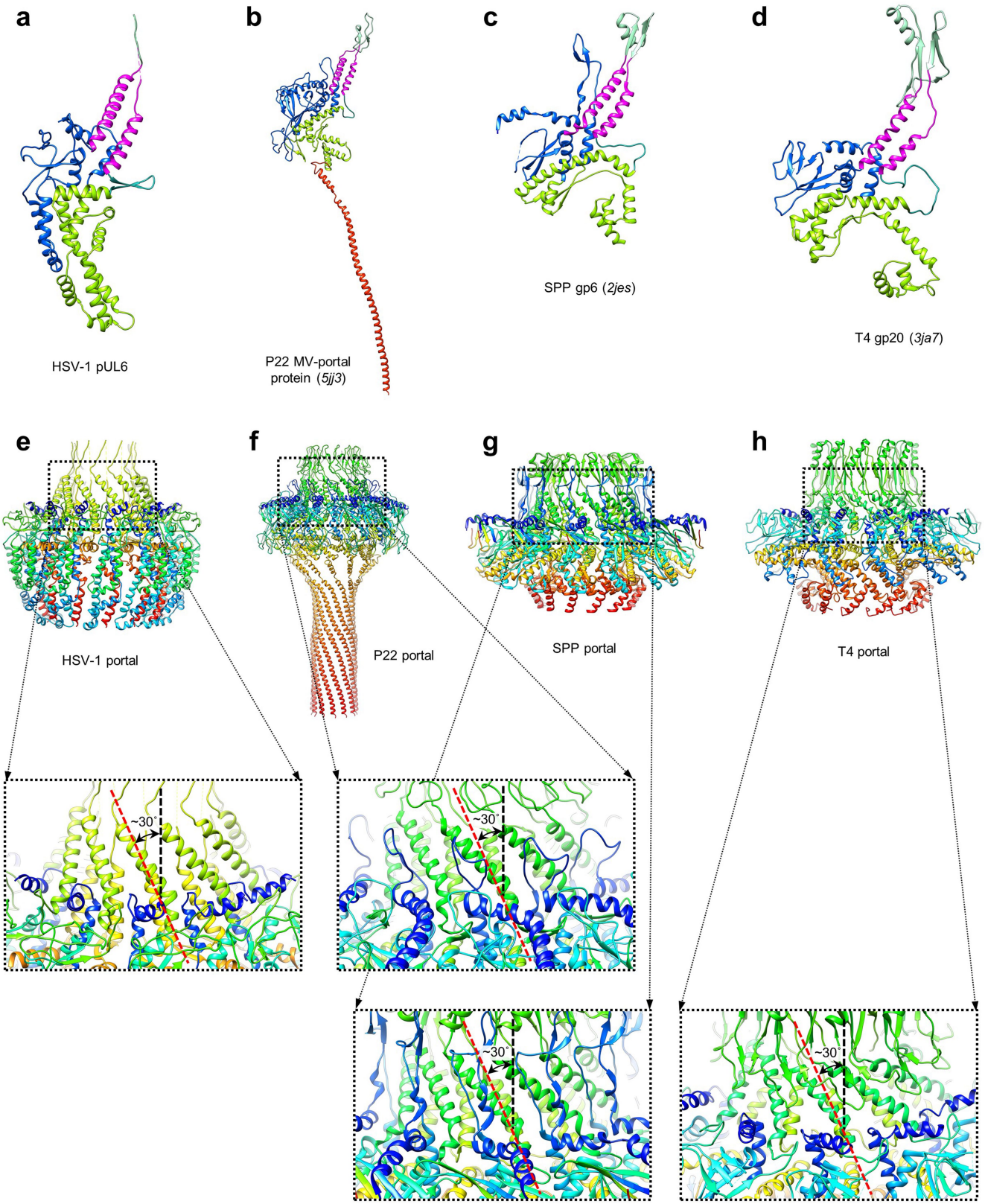

Extended Data Fig. 5 | pUL6 portal protein homologues. a–d, HSV-1 pUL6 and pUL6 homologues coloured analogously by pUL6 domain. **e–h**, HSV-1 pUL6 portal complex and homologues coloured in rainbow (red (N terminus) to blue (C terminus)). Respective insets illustrate the conserved left-handed corkscrew of stem helices in the portal channel beneath the clip.

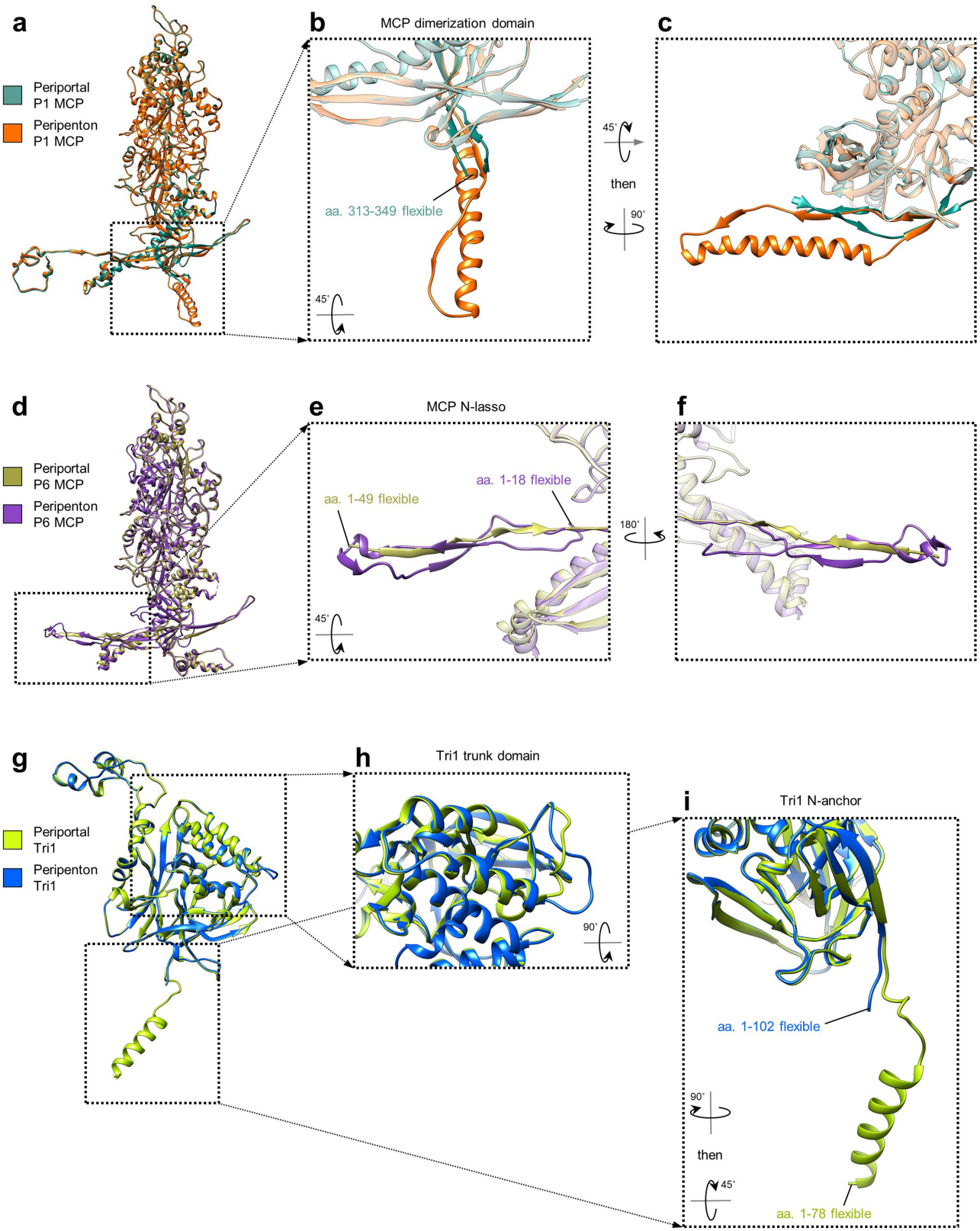

Extended Data Fig. 6 | Comparison of periportal and peripenton capsid proteins. a–c, Comparison of periportal and peripenton P1 MCPs (**a**) reveal conformational differences in their dimerization domains (**b**, **c**). **d–f**, Comparison of periportal and peripenton P6 MCPs (**d**) reveal conformational differences in their N-lassos (**e**, **f**). **g–i**, Comparison of periportal and peripenton Tri1s (**g**) reveal differences in a trunk loop where periportal Tri1 interfaces with tentacle helices (**h**) and a visible N-anchor helix in periportal Tri1 (**i**).

Extended Data Table 1 | Cryo-EM parameters and statistics

CryoEM data collection, refinement, and validation statistics

	C5 portal vertex reconstruction (EMDB-9860) (PDB-6ODM)	C12 portal reconstruction (EMDB-9862) (PDB-6OD7)	C1 virion reconstruction (EMDB-9864)	C1 portal vertex reconstruction (EMDB-9861)	C1 terminal DNA & portal vertex reconstruction (EMDB-9863)
Data collection and processing					
Magnification	14000	14000	14000	14000	14000
Voltage (kV)	300	300	300	300	300
Electron exposure (e^-/Å^2)	25	25	25	25	25
Defocus range (μm)	-1 to -3	-1 to -3	-1 to -3	-1 to -3	-1 to -3
Pixel size (Å)	1.03	1.03	2.06	1.03	1.03
Symmetry imposed	C5	C12	C1	C1	C1
Initial particle images (no.)	45,445	45,445	45,445	45,445	45,445
Final particle images (no.)	42,857	39,939	39,939	39,939	34,132
Map resolution (Å)	4.3	5.6	6.2	5.4	10.1
FSC threshold	0.143	0.143	0.143	0.143	0.143
Map resolution range (Å)	3.5-5.5	4-6	5-30	4-8	8-16
Refinement					
Initial model used (PDB code)	--	--	--	--	--
Model resolution (Å)					
FSC threshold					
Model resolution range (Å)					
Map sharpening B factor (Å^2)	100	250			
Model composition					
Non-hydrogen atoms	--	--			
Protein residues	8,562	4,596			
Ligands	--	--			
B factors (Å^2)					
Protein	144.05	157.06			
Ligand	--	--			
R.m.s. deviations					
Bond lengths (Å)	0.005	0.008			
Bond angles (°)	0.921	1.145			
Validation					
MolProbity score	1.69	1.89			
Clashscore	5.66	9.73			
Poor rotamers (%)	0.23%	0.92%			
Ramachandran plot					
Favored (%)	94.45%	94.46%			
Allowed (%)	5.29%	5.54%			
Disallowed (%)	0.26%	0.00%			

cryo-EM data collection, refinement and validation statistics are shown. Atomic models were iteratively refined using real-space refinement in Phenix[45].

nature research

Corresponding author(s): ZH Zhou

Reporting Summary

Nature Research wishes to improve the reproducibility of the work that we publish. This form provides structure for consistency and transparency in reporting. For further information on Nature Research policies, see Authors & Referees and the Editorial Policy Checklist.

Statistical parameters

When statistical analyses are reported, confirm that the following items are present in the relevant location (e.g. figure legend, table legend, main text, or Methods section).

n/a	Confirmed
☒	☐ The exact sample size (*n*) for each experimental group/condition, given as a discrete number and unit of measurement
☒	☐ An indication of whether measurements were taken from distinct samples or whether the same sample was measured repeatedly
☒	☐ The statistical test(s) used AND whether they are one- or two-sided *Only common tests should be described solely by name; describe more complex techniques in the Methods section.*
☒	☐ A description of all covariates tested
☒	☐ A description of any assumptions or corrections, such as tests of normality and adjustment for multiple comparisons
☒	☐ A full description of the statistics including central tendency (e.g. means) or other basic estimates (e.g. regression coefficient) AND variation (e.g. standard deviation) or associated estimates of uncertainty (e.g. confidence intervals)
☒	☐ For null hypothesis testing, the test statistic (e.g. *F*, *t*, *r*) with confidence intervals, effect sizes, degrees of freedom and *P* value noted *Give P values as exact values whenever suitable.*
☒	☐ For Bayesian analysis, information on the choice of priors and Markov chain Monte Carlo settings
☒	☐ For hierarchical and complex designs, identification of the appropriate level for tests and full reporting of outcomes
☒	☐ Estimates of effect sizes (e.g. Cohen's *d*, Pearson's *r*), indicating how they were calculated
☒	☐ Clearly defined error bars *State explicitly what error bars represent (e.g. SD, SE, CI)*

Our web collection on statistics for biologists may be useful.

Software and code

Policy information about availability of computer code

Data collection	Leginon
Data analysis	EMAN, CTFFIND3, RELION2.1, UCSF Chimera, Resmap, Molprobity, Coot, PHENIX, MDFF, Phyre2

For manuscripts utilizing custom algorithms or software that are central to the research but not yet described in published literature, software must be made available to editors/reviewers upon request. We strongly encourage code deposition in a community repository (e.g. GitHub). See the Nature Research guidelines for submitting code & software for further information.

Data

Policy information about availability of data

All manuscripts must include a data availability statement. This statement should provide the following information, where applicable:

- Accession codes, unique identifiers, or web links for publicly available datasets
- A list of figures that have associated raw data
- A description of any restrictions on data availability

Atomic models and cryoEM density maps have been deposited to the Protein Data Bank and the Electron Microscopy Data Bank, under the accession numbers PDB-6ODM and PDB-6OD7; and EMD-9860, EMD-9861, EMD-9862, EMD-9863, and EMD-9864; respectively.

Field-specific reporting

Please select the best fit for your research. If you are not sure, read the appropriate sections before making your selection.

☒ Life sciences ☐ Behavioural & social sciences ☐ Ecological, evolutionary & environmental sciences

For a reference copy of the document with all sections, see nature.com/authors/policies/ReportingSummary-flat.pdf

Life sciences study design

All studies must disclose on these points even when the disclosure is negative.

Sample size	3D reconstructions were calculated from appr. 40,000 particle images, determined as necessary based on target resolutions sufficient to reveal different amino acid residue sidechains. Final resolutions were estimated by the Resmap program to be appr. 4.3 angstroms.
Data exclusions	None
Replication	Reconstructions are the result of calculations performed on the collected data set. Therefore, all reconstructions are reproducible if the workflow is maintained.
Randomization	Randomization is not relevant to our study as no (experimentally selected) groups are involved.
Blinding	Blinding is not relevant to our study as reconstruction algorithms and data processing preclude trial bias.

Reporting for specific materials, systems and methods

Materials & experimental systems

n/a	Involved in the study
☒	☐ Unique biological materials
☒	☐ Antibodies
☒	☐ Eukaryotic cell lines
☒	☐ Palaeontology
☒	☐ Animals and other organisms
☒	☐ Human research participants

Methods

n/a	Involved in the study
☒	☐ ChIP-seq
☒	☐ Flow cytometry
☒	☐ MRI-based neuroimaging